ChemPubSoc Europe

DOI: 10.1002/chem.201304700

CHEMISTRY
A European Journal
Full Paper

Hybrid Nanomaterials

Supercritical Carbon Dioxide Assisted Deposition of Fe_3O_4 Nanoparticles on Hierarchical Porous Carbon and Their Lithium-Storage Performance

Lingyan Wang,[a, b, c] Linhai Zhuo,*[d] Chao Zhang,[a, b] and Fengyu Zhao*[a, b]

Abstract: A composite of highly dispersed Fe_3O_4 nanoparticles (NPs) anchored in three-dimensional hierarchical porous carbon networks (Fe_3O_4/3DHPC) as an anode material for lithium-ion batteries (LIBs) was prepared by means of a deposition technique assisted by a supercritical carbon dioxide ($scCO_2$)-expanded ethanol solution. The as-synthesized Fe_3O_4/3DHPC composite exhibits a bimodal porous 3D architecture with mutually connected 3.7 nm mesopores defined in the macroporous wall on which a layer of small and uniform Fe_3O_4 NPs was closely coated. As an anode material for LIBs, the Fe_3O_4/3DHPC composite with 79 wt% Fe_3O_4 (Fe_3O_4/3DHPC-79) delivered a high reversible capacity of 1462 mA h g^{-1} after 100 cycles at a current density of 100 mA g^{-1}, and maintained good high-rate performance (728, 507, and 239 mA h g^{-1} at 1, 2, and 5 C, respectively). Moreover, it showed excellent long-term cycling performance at high current densities, 1 and 2 A g^{-1}. The enhanced lithium-storage behavior can be attributed to the synergistic effect of the porous support and the homogeneous Fe_3O_4 NPs. More importantly, this straightforward, highly efficient, and green synthetic route will definitely enrich the methodologies for the fabrication of carbon-based transition-metal oxide composites, and provide great potential materials for additional applications in supercapacitors, sensors, and catalyses.

Introduction

Ever since nanosized transition-metal oxides were reported as alternative negative electrode materials for lithium-ion batteries (LIBs) in 2000,[1] enormous research efforts have been devoted to the design and applications of transition-metal oxides (MO_x; M: Fe, Co, Ni, and so forth) and their composites on account of the "conversion reaction" process and their high theoretical capacities.[2] To alleviate the problems of poor electronic conductivity, poor cycling performance, and the aggregation of transition-metal oxide based electrode materials, one efficient strategy is to load nanometer-sized transition-metal oxide onto the carbon-based matrix.[3] Thus, a variety of carbonaceous materials such as porous carbon materials, carbon nanotubes (CNTs), and graphene (GE) are usually used as promising candidates to form various carbon-based metal oxide composites by means of precipitation,[4] hydrothermal/solvothermal methods,[5] hydrolyzation,[6] thermal decomposition,[7] and so on. However, these traditional methods always suffer from some drawbacks. On the one hand, to obtain satisfactory adhesion and realize controllable coverage of metal oxide over the carbon matrix, it is often necessary to pretreat or modify the carbon matrix to produce functional groups on its surface. For example, harsh oxidative pretreatment or modification with surfactant is needed for the CNTs because of the intrinsic poor solubility and processability,[8] and oxidative treatment is necessary for GE owing to the lack of functional groups on its surface.[9] Unfortunately, such drastic oxidative conditions inevitably damage the sp^2 structure, and the electronic characteristics of CNTs or GE and involve complicated process control.[9a] On the other hand, the traditional preparation methods generally employ large quantities of organic solvents that could burden the post-treatment and bring about some unexpected environmental problems.[10] More importantly, either primary precursors or intermediates generated in the traditional procedures tend to form crystalline metal oxide particles. Since the crystallization involves nucleation and anisotropic growth of primary particles, the formed crystalline seeds tend to aggregate into large units in polar solvents, such as

[a] Dr. L. Wang, Dr. C. Zhang, Prof. Dr. F. Zhao
State Key Laboratory of Electroanalytical Chemistry
Changchun Institute of Applied Chemistry
Chinese Academy of Sciences
Changchun 130022 (P.R. China)
Fax: (+86) 431-85262410
E-mail: zhaofy@ciac.ac.cn

[b] Dr. L. Wang, Dr. C. Zhang, Prof. Dr. F. Zhao
Laboratory of Green Chemistry and Process
Changchun Institute of Applied Chemistry
Chinese Academy of Sciences
Changchun 130022 (P.R. China)

[c] Dr. L. Wang
University of the Chinese Academy of Sciences
Beijing 100049 (P.R. China)

[d] Dr. L. Zhuo
College of Chemistry and Chemical Engineering
Taishan University, Taian 271021 (P.R. China)
E-mail: zhuoling77@163.com

Supporting information for this article is available on the WWW under http://dx.doi.org/10.1002/chem.201304700.

ethanol or water, owing to their high surface energy.[9b,c] Whereas nonpolar solvents usually have high viscosity, high surface tension, and low diffusivity, they strongly limit the ability of solvents to homogeneously disperse the precursor onto the surface of the substrate, thereby resulting in poor adhesion or the formation of freely aggregated particles in solution.[5b,11] Therefore, it is a considerable challenge to explore an effective and green approach to realize the uniform dispersion of guest components onto the carbon-based support.

As a green and sustainable technology, deposition of supercritical carbon dioxide ($scCO_2$) offers an elegant and efficient route for the synthesis and processing of novel nanomaterials.[12] $scCO_2$ is an attractive alternative to organic solvents as it is nontoxic, nonflammable, inexpensive, naturally abundant, and chemically inert.[13] Its physical properties such as density and solvent power can be easily tuned by adjusting the operating temperature and pressure. Low-viscosity, near-zero surface tension, and high diffusivity of $scCO_2$ are considered highly favorable properties for synthesizing superior ultrafine and uniform nanomaterials and increasing reaction rates.[14] Simultaneously, the $scCO_2$ deposition technique shows superior advantages in the processing of cellular materials, because it can largely mitigate the mass-transfer limitation, facilitate the infiltration of precursor in the complex geometries, and maintain the porous nanostructure without collapsing.[13a,14a,15] In addition, $scCO_2$ as an antisolvent could reduce the solvent strength caused by hydroxyl groups that originate from ethanol and water, and thus greatly lower the aggregation of the final particles.[9a,12a] Therefore, the $scCO_2$ deposition technique could efficiently overcome the common difficulties in traditional deposition methods and realize a uniform, accurate, and controllable coating.

Herein, we develop a straightforward, highly efficient, and green synthetic route to prepare monodisperse Fe_3O_4 nanoparticles (NPs) on a 3DHPC matrix through in situ reaction of the precursor in $scCO_2$-expanded ethanol. Fe_3O_4 was used as the model system owing to its high theoretical capacity (926 mA h g^{-1}), low cost, natural abundance, and environmental friendliness.[16] The 3D macroporous carbon with interconnected mesoporous walls can not only facilitate the rapid transport of Li^+ ions into the interior of the bulk material, but also provides a high surface area for available charge-storage sites and the ion adsorption.[17] In addition, the special structure can efficiently accommodate the volume change of Fe_3O_4 and prevent its aggregation during cycling. As a result, the Fe_3O_4/3DHPC composite exhibited high reversible capacity, excellent cycling stability, and good rate capability when tested as an anode material for LIBs.

Results and Discussion

Figure 1a illustrates the synthetic procedure of the Fe_3O_4/3DHPC composite. Firstly, the 3DHPC matrix was prepared by a dual-templating approach with the solvent-evaporation-induced surfactant assembly (EISA) process, by employing ordered silica colloidal crystals as hard templates, F127 as a soft template, and soluble resols as carbon source.[18] Briefly, monodisperse silica microspheres are packed into a 3D colloidal crystal array by sedimentation. A solution that contained resols and F127 in ethanol was then soaked into the voids of colloidal silica monolith, and the organic–organic self-assembly of the resins and F127 occurred during the evaporation of ethanol, thereby resulting in the formation of ordered mesostructure in the interstitial voids. Further heating at 100 °C for thermosetting of phenolic formaldehyde (PF) resulted in the formation of silica/PF/F127 composites. Subsequently, the composites were subjected to pyrolysis in N_2 at 800 °C, during which the F127 decomposed, and the phenolic resin framework carbonized, thus leading to silica/carbon composites. Finally, 3DHPC was obtained after the removal of the silica by HF solution. Subsequently, the $Fe(NO_3)_3$ ethanol solution was expended by introducing 12.0 MPa CO_2 to form a homogeneous fluid. Owing to the low viscosity and high diffusivity of $scCO_2$ together with its near-zero surface tension, it largely mitigates the mass-transfer limitation and facilitates the thorough infiltration of Fe^{3+} into the macropores of the 3DHPC matrix. Once the temperature is increased, the soluble precursor begins to decompose and deposits onto the wall of the matrix uniformly.[19] The physicochemical properties of such a specific fluid could facilitate the nucleation/transfer/deposition of such solid compounds, thereby minimizing the formation of free particles and thus leading to a perfect coating. Finally, the iron oxide was obtained after thermal treatment.

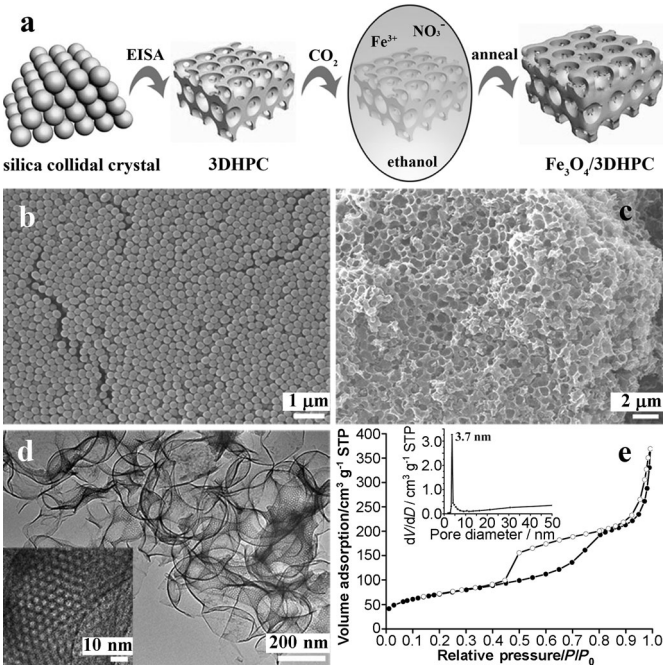

Figure 1. a) Schematic diagram of the fabrication of Fe_3O_4/3DHPC; b) SEM image of silica spheres; c–e) SEM, TEM (inset shows the high-resolution TEM image), N_2 adsorption–desorption isotherms, and the corresponding pore-size distribution (inset) of the as-synthesized 3DHPC, respectively.

Figure 1b shows the typical SEM image of silica spheres with a uniform diameter around 220 nm. Figure 1c displays the as-prepared 3DHPC with regular 3D arrays of interconnected cellular networks. On the basis of the SEM image, the average

pore spacing and wall thickness are approximately 200 and 30 nm, respectively. Meanwhile, the TEM and high-resolution (HR)TEM images (Figure 1d) clearly demonstrate the presence of both well-defined mesopores and macropores in a multiple overlapping shape, thereby suggesting that the macropores and neighboring ones are closely interconnected in a 3D continuous network of the carbon replica. The diameter of the macropores measured from the TEM image is about 200 nm, which suggests a slight shrinkage. Additionally, the HRTEM view further reveals that the wall of macropores is composed of mutually connected and well-organized spherical mesopores of approximately 4 nm. We believe that the unique bimodal pore structure is beneficial for improving the lithium-storage performance, because the diffusion of Li^+ ions strongly depends on the transport length and accessible sites on the surface of active materials.[4] Figure 1e presents the N_2 adsorption–desorption isotherm together with pore-size distribution of the 3DHPC matrix. A characteristic type IV isotherm, with a pronounced narrow capillary condensation step and a uniform pore distribution, is observed, and displays two hysteresis loops. The hysteresis loop at low relative pressure of 0.40–0.85 is of type H2, which can be ascribed to capillary condensation in mesopores generated by copolymer F127. The other loop, which is at a higher pressure of 0.85–1.0, has a type-H3 shape, and this might be on account of interparticle pores within the sample.[20] The specific surface area (S_{BET}) and the pore volume (V_t) are 249 $m^2 g^{-1}$ and 0.40 $cm^3 g^{-1}$, respectively. Moreover, on the basis of the Barrett–Joyner–Halenda model, the 3DHPC matrix exhibits a narrow Gaussian pore-size distribution centered at 3.7 nm (the inset of Figure 1e), which corresponds with the results of HRTEM.

To ascertain the component and structure of the products, XRD and X-ray photoelectron spectroscopy (XPS) measurements were performed. Figure 2a depicts the XRD patterns of the samples prepared in pure ethanol or in the presence of CO_2. The diffraction peaks match the magnetite Fe_3O_4 (JCPDS no. 75-0449) and maghemite Fe_2O_3 (JCPDS no. 39-1346) phases for all the samples. Accordingly, XPS measurements were used to further confirm the chemical composition, since XPS is useful to distinguish between Fe^{2+} and Fe^{3+} cations. As shown in Figure 2b, the survey spectrum of the Fe_3O_4/3DHPC-79 sample reveals the presence of C, Fe, and O. The high-resolution XPS spectrum for the Fe 2p is a typical core-level spectrum of Fe_3O_4 with broad peaks around 710.4 and 724.3 eV that correspond to Fe $2p_{3/2}$ and Fe $2p_{1/2}$, respectively. In addition, no satellite peak can be identified; it eliminates the presence of Fe_2O_3.[21] Hence, we can conclude that the final products are Fe_3O_4 phase. Additionally, the average particle size of Fe_3O_4 in Fe_3O_4/3DHPC-65, Fe_3O_4/3DHPC-79, and Fe_3O_4/3DHPC-86 is 12.1, 12.5, and 12.9 nm, respectively, as calculated from the largest diffraction peak (311) by using the Debye–Scherer formula. However, the particle size formed in pure ethanol without introducing CO_2 (Fe_3O_4/3DHPC-E-79) is larger than these formed in the $scCO_2$-expanded ethanol; it is about 17.6 nm.

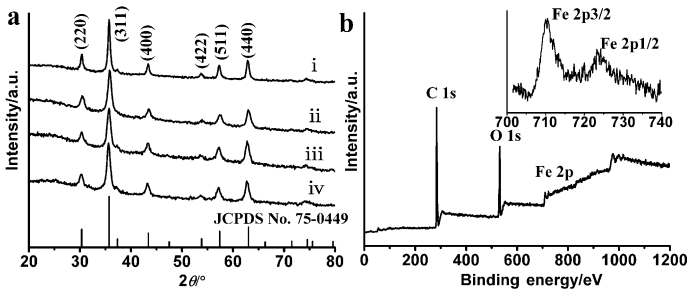

Figure 2. a) XRD patterns of i) Fe_3O_4/3DHPC-E-79, ii) Fe_3O_4/3DHPC-65, iii) Fe_3O_4/3DHPC-79, and iv) Fe_3O_4/3DHPC-86. b) Wide-survey XPS and high-resolution Fe 2p XPS spectra (inset) of the Fe_3O_4/3DHPC-79 sample.

The morphology and microstructure of Fe_3O_4/3DHPC composites were characterized by SEM and TEM. The SEM images clearly showed that a continuous and uniform Fe_3O_4 layer was coated on the surface of the interconnected porous 3DHPC network, and no free Fe_3O_4 NPs were formed even at a high loading of 86 wt% (Figure 3a–c), directly suggesting the efficiency of CO_2-expanded solution deposition. In other words, the loading or thickness of Fe_3O_4 layer on the matrix could be finely controlled to achieve a desirable amount, and the formation of free Fe_3O_4 NPs could be successfully avoided in the $scCO_2$-expanded ethanol system. By contrast, Fe_3O_4/3DHPC-E-79 synthesized in pure ethanol showed a large amount of free Fe_3O_4 particles, which fail to attach onto the surface of 3DHPC (Figure S2a in the Supporting Information). Furthermore, elemental mapping of Fe_3O_4/3DHPC-79 on C, Fe, and O further demonstrates the uniform dispersion of iron on the composite, namely, the uniform dispersion of Fe_3O_4 particles on the 3DHPC. In the TEM image it is clearly seen that the Fe_3O_4 was distributed in the form of individual particles approximately 11–15 nm in diameter (Figure 3e), which stood in stark contrast to the sample of Fe_3O_4/3DHPC-E-79 obtained in pure ethanol, in which a large amount of Fe_3O_4 particles attached onto the matrix were aggregated (Figure S2b in the Supporting Information), and a great number of free Fe_3O_4 particles were observed in solution (Figure S2c in the Supporting Information). The HRTEM image (Figure 3f) also confirmed that the Fe_3O_4 NPs in the Fe_3O_4/3DHPC-79 composite were highly dispersed with well-textured and single-crystalline nature.

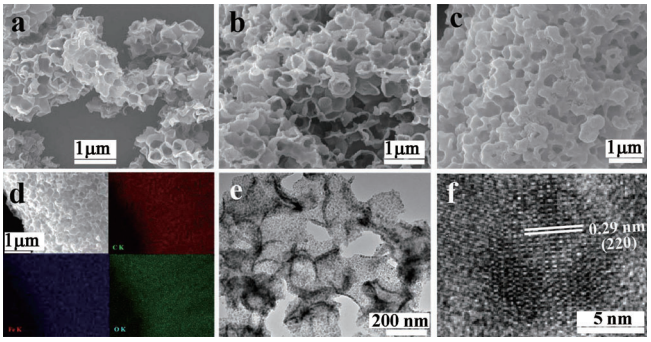

Figure 3. SEM images of a) Fe_3O_4/3DHPC-65, b) Fe_3O_4/3DHPC-79, and c) Fe_3O_4/3DHPC-86. d–f) Elemental mapping images, TEM, and HRTEM images of Fe_3O_4/3DHPC-79, respectively.

In addition, the Fe_3O_4-loaded composites were also investigated by N_2 adsorption–desorption isotherms together with pore-size distributions (Figure S3 in the Supporting Information). The results showed that these isotherms were close to type IV with an evident hysteresis loop at a relative pressure of 0.4–1.0, thus indicating a mesoporous structure of the Fe_3O_4/3DHPC composites. In addition, all samples showed the same mesopore size distribution as the matrix centered at 3.7 nm, which suggests that most Fe_3O_4 NPs were anchored on the macropores of the 3DHPC. According to Table S1 in the Supporting Information, the S_{BET} and V_t of Fe_3O_4/3DHPC samples after being decorated with Fe_3O_4 significantly decreased. But there is an interesting phenomenon that the coating has little impact on the S_{BET} and V_t values for Fe_3O_4/3DHPC-X (X is the Fe_3O_4 content) composites synthesized with $scCO_2$. We speculate that the S_{BET} and V_t are largely influenced by the micropores and mesopores; the Fe_3O_4 NPs obtained by means of the $scCO_2$ technique were uniformly anchored on the macropores of the 3DHPC to form a compact, thin coating layer. Thus, the change in Fe_3O_4 content slightly changed the thickness of the coating layer, but not the S_{BET} and V_t.

The above results indicate that $scCO_2$-expanded ethanol is an effective medium for coating the guest components onto the matrix with high efficiency. In this work, compressed CO_2 was introduced into the vessel and dissolved into ethanol accompanied by volume expansion of the solution. Then a stable solid compound coordinated by bridged oxygen between Fe^{3+} and NO_3^{2-} and CO_3^{2-}, together with H_2O, precipitated onto the matrix from the fluid.[14d] At the same time, $scCO_2$ as an antisolvent reduced the solvent polarity caused by hydroxyl groups that originated from ethanol and crystal water, thus leading to the intermediate forming with amorphous structure but not anisotropic growth (Figure S4a in the Supporting Information),[22] and thus small and uniform particles covered the surface of the matrix. However, in pure ethanol, the existence of surface tension and hydroxyl groups as well as low diffusivity strongly limited the intermediate coating onto the surface of substrate, thereby resulting in the guest components crystallizing and aggregating freely in solution (Figure S4b and Figure S2 in the Supporting Information).

To identify all of the electrochemical reactions, cyclic voltammetry (CV) was conducted on the cells of Fe_3O_4/3DHPC-79 and Fe_3O_4/3DHPC-E-79 along with those of pure 3DHPC and commercial Fe_3O_4 in Figure 4. As shown in Figure 4a, a broad reduction peak occurred around 0.6 V during the first cathodic process of 3DHPC, and it disappeared in the following cycles. This peak could be ascribed to the electrolyte decomposition on the fresh surface of the carbon material and the formation of solid electrolyte interface (SEI). For the Fe_3O_4-based materials (Figure 4b–d), there was a peak located at 1.5 V in the first cycle, and it could be ascribed to the reduction of the irreversible reaction with the electrolyte. The peaks observed at approximately 0.8 and 0.6 V represented two steps of the lithiation reactions of Fe_3O_4 ($Fe_3O_4 + xLi^+ + xe^- \rightarrow Li_xFe_3O_4$; $Li_xFe_3O_4 \rightarrow Fe^0 + Li_2O$) and the irreversible reaction with the electrolyte.[23] In the anodic process, the Fe_3O_4/3DHPC-79 electrode showed multiple anodic peaks between 1.65 and 2.0 V,

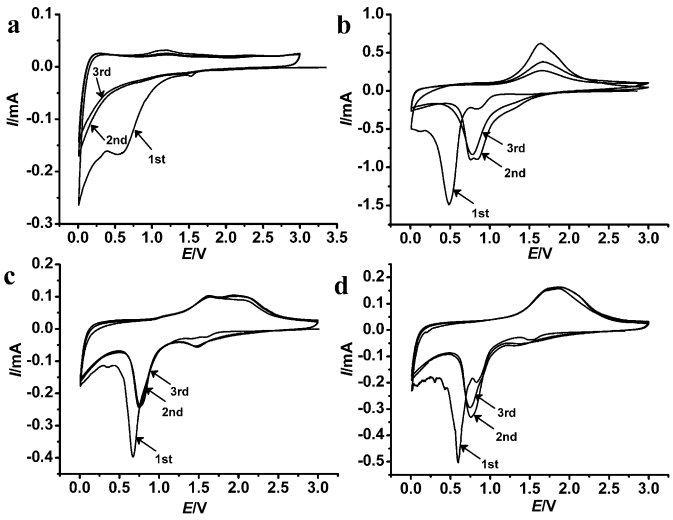

Figure 4. Cyclic voltammograms of a) 3DHPC, b) commercial Fe_3O_4, c) Fe_3O_4/3DHPC-79, and d) Fe_3O_4/3DHPC-E-79.

which indicated that the oxidation might occur from Fe^0 to Fe^{2+} and Fe^{3+} in two steps.[3b,24] But these peaks were not observed in the commercial Fe_3O_4 or Fe_3O_4/3DHPC-E-79 samples, and instead a wide peak was visible around 1.65 V. From the second cycle, both cathodic and anodic peaks shifted positively, which was ascribed to the polarization of the electrode materials in the first cycle.[24,25] The CV measurements therefore indicated good electrochemical activity and stability of Fe_3O_4/3DHPC-79 composite relative to Fe_3O_4/3DHPC-E-79 and commercial Fe_3O_4.

Figure 5a and b show the charge/discharge voltage profiles of Fe_3O_4/3DHPC-79 and Fe_3O_4/3DHPC-E-79 electrodes. Both the discharge voltage profiles exhibited a short sloping region above approximately 1 V and a subsequent plateau at approximately 0.8 V, followed by a long sloping line down to 0 V, which agreed with CV measurements. But the charge/discharge capacities were totally different from the above two samples. The Fe_3O_4/3DHPC-79 electrode delivered a very high lithium-storage capacity of 1768 mA h g^{-1} at the initial discharge process, and the reversible capacity was 1076 mA h g^{-1}, which led to an irreversible capacity loss of 39%. By contrast, the initial discharge and charge capacity of the Fe_3O_4/3DHPC-E-79 electrode were 1337 and 840 mA h g^{-1}, respectively, thus leading to an irreversible capacity loss of 37%. The large irreversible capacity observed in the first cycle might be caused by the conversion of Fe_3O_4 to Fe NPs, along with the formation of amorphous Li_2O and SEI. In subsequent cycles, the Fe_3O_4/3DHPC-79 showed excellent capacity retention, whereas the Fe_3O_4/3DHPC-E-79 electrode decreased rapidly with subsequent cycles.

The durability of Fe_3O_4/3DHPC composites was assessed by cycling in the range of 0.01–3.0 V at 100 mA g^{-1}, and commercial Fe_3O_4 and 3DHPC were also included for comparison. As displayed in Figure 5c, the Fe_3O_4/3DHPC-X electrodes demonstrated higher reversible capacities than those of pure 3DHPC and commercial Fe_3O_4. In the first cycle, the discharge capacity of the commercial Fe_3O_4 electrode was 1237 mA h g^{-1}, but it

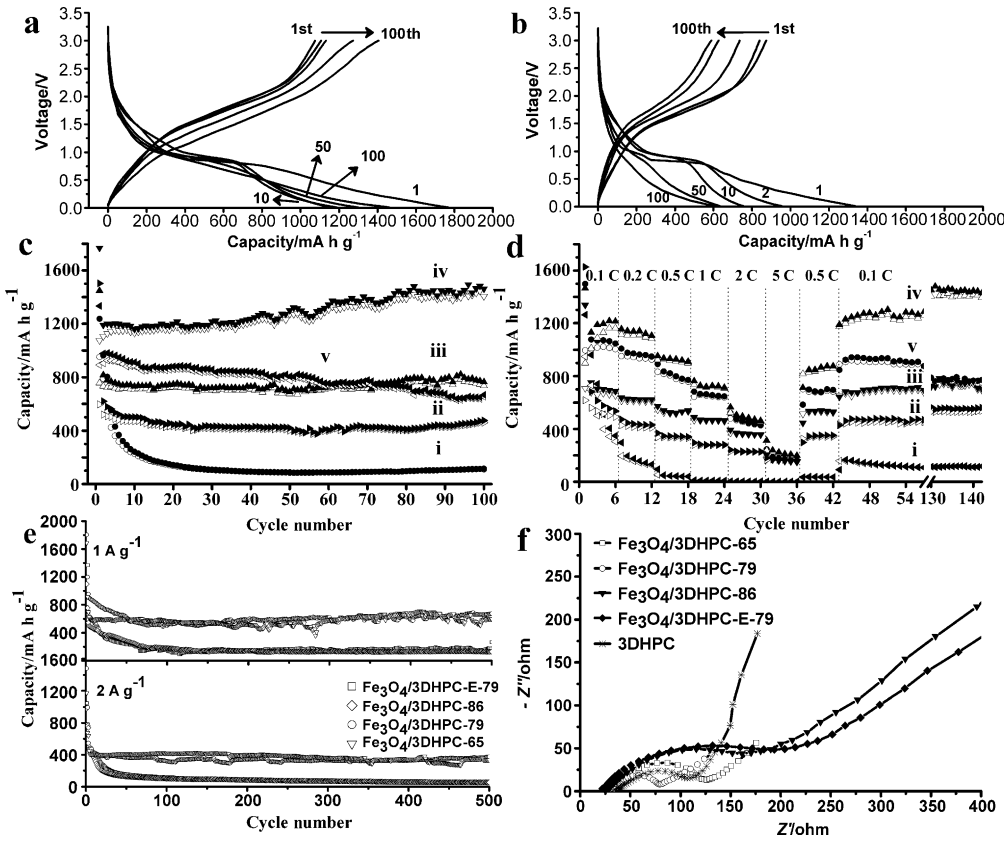

Figure 5. The charge/discharge voltage profiles of a) Fe_3O_4/3DHPC-79 and b) Fe_3O_4/3DHPC-E-79 at 100 mA g^{-1}. c) Cycling and d) rate performances of i) commercial Fe_3O_4, ii) bare 3DHPC, iii) Fe_3O_4/3DHPC-65, iv) Fe_3O_4/3DHPC-79, and v) Fe_3O_4/3DHPC-86. e) Long-life cycling tests of Fe_3O_4/3DHPC electrodes. f) Nyquist plots of all electrodes after 100 cycles at 100 mA g^{-1} in the frequency range from 100 kHz to 100 mHz (1 C = 926 mA g^{-1}).

continuously decreased and reached 114 mA h g^{-1} after 100 cycles, which was only 12% of the initial reversible capacity, thus indicating poor capacity retention. For the 3DHPC, it showed an average discharge capacity of 440 mA h g^{-1} with an excellent cycling stability, which indicates that 3D architecture benefits the cycle stability. Interestingly, after being decorated on 3DHPC, the Fe_3O_4 NPs presented excellent cyclic performance. The capacity of the Fe_3O_4/3DHPC-65 composite reached 764 mA h g^{-1} after 100 cycles, and retained 94% of the initial reversible capacity (817 mA h g^{-1}). Surprisingly, the best cyclic stability was achieved by the Fe_3O_4/3DHPC-79 composite. It gave a reversible capacity of 1462 mA h g^{-1} with as high as 123% retention of the initial reversible capacity over 100 cycles. This interesting phenomenon of capacity rise with cycling has been observed by other researchers on carbon/iron oxide.[6c,25,26] It could be attributed to the reversible growth of a polymer/gel-like layer by electrolyte decomposition at low potential through a so-called "pseudocapacitance-type behavior".[1,27] By contrast, the Fe_3O_4/3DHPC-E-79 electrode showed inferior cycle stability, and its discharge capacity dramatically dropped to 756 mA h g^{-1} upon the tenth cycle from 1337 mA h g^{-1} of the first cycle, and finally reached 608 mA h g^{-1} upon the 100th cycle (Figure S5a in the Supporting Information). However, increasing the Fe_3O_4 content from 79 to 86% led to poor cycling stability, for which one of the reasonable explanations is that the thicker coating will result in the shrinkage of the void space and cannot efficiently mitigate the mechanical stress of Fe_3O_4 NPs generated during the charge/discharge process, which furthermore destroys the structural integrity and cycling stability of the electrode.

Figure 5d and Table S2 in the Supporting Information show the rate performances at stepwise current-rate range of 0.1–5 C, then back to 0.5 and 0.1 C for another 100 cycles. Relative to commercial Fe_3O_4, Fe_3O_4/3DHPC composites exhibit enhanced rate performances. For the 3DHPC matrix, its capacity decreased slowly with increasing rates, and recovered the original capacity when the rate returned to the initial stage. The result further confirms that hierarchically porous carbon can serve as a good model for the design of materials for high-performance LIBs.[28] In addition, the Fe_3O_4/3DHPC-79 electrode exhibited the highest rate performance and cycling stability relative to Fe_3O_4/3DHPC-65 and Fe_3O_4/3DHPC-86 electrodes. As the current density increased in stages from 0.1 to 1 C, the reversible capacities of Fe_3O_4/3DHPC-79 gradually decreased from 1219 to 1142, 936, and 728 mA h g^{-1}. Even at high rates (i.e., 2 and 5 C), the electrode still retained 507 and 240 mA h g^{-1}, respectively. The charge/discharge curves still maintain the kinetics feature at high rates relative to low rates, thus indicating a facile charge-transport process. More importantly, an average capacity as high as 1409 mA h g^{-1} could be resumed when the current rate returned to 0.1 C, which suggests the good structural stability of the Fe_3O_4/3DHPC-79 electrode. Relative to Fe_3O_4/3DHPC-79, higher Fe_3O_4 loading (86 wt%) resulted in poorer rate performance. The thicker coating not only increases the transport length of Li^+ ions, which greatly contributes to improving the rate performance, but also puts the outer Fe_3O_4 NPs layer in weaker contact with the conductive support and decreases the electron conductivity of the overall electrode. At the same time, the decreased void space cannot efficiently mitigate the mechanical stress of Fe_3O_4 NPs generated during the charge/discharge process. However, the lower Fe_3O_4 content in the composite accounts for the lower lithium-storage performance of Fe_3O_4/3DHPC-65, since the theoretical specific capacity (C) is calculated according to the theoretical capacity of Fe_3O_4 (926 mA h g^{-1}) and the largest reversible capacity of 3DHPC (596 mA h g^{-1}) (i.e., $C = 926 \times X + 596 \times (1 - X)$). But

in the case of Fe_3O_4/3DHPC-E-79 (Figure S5 in the Supporting Information), the reversible capacity decreased from 935 to 744, 437, 218, 97, and 39 mA h g^{-1} when the current density increased from 0.1 to 0.2, 0.5, 1, 2, and 5 C, respectively, which indicates much poorer rate capability and stability.

To further evaluate the electrochemical performance of Fe_3O_4/3DHPC composites, we investigated the long-term cycling performances at high current densities of 1 and 2 A g^{-1} for up to 500 cycles after the first three cycles at 100 mA g^{-1} (Figure 5e). Overall, Fe_3O_4/3DHPC-65 and Fe_3O_4/3DHPC-79 samples showed capacities that far exceeded those of Fe_3O_4/3DHPC-86 and Fe_3O_4/3DHPC-E-79. The specific capacity of Fe_3O_4/3DHPC-86 electrode after 500 cycles was 131 mA h g^{-1} at 1 A g^{-1} and 55 mA h g^{-1} at 2 A g^{-1}, respectively. For the Fe_3O_4/3DHPC-79 sample, the specific capacity decreased slightly to 526 mA h g^{-1} after 70 cycles at 1 A g^{-1}, and then, interestingly, its capacity gradually increased to 676 mA h g^{-1} after 500 cycles. It is noteworthy that the Fe_3O_4/3DHPC-65 showed a similar capacity to that of Fe_3O_4/3DHPC-79, and it exhibited better capacity retention, with 95% capacity of the fourth cycle at 1 A g^{-1} after 500 cycles, which is better than 75% for Fe_3O_4/3DHPC-79. The results prove that the thinner coating layer benefits retention of the excellent capability and stability at high rates owing to a simultaneously reduced inner resistance and efficient ion-transportation pathways.

To clarify the difference in electrochemical performance among all the samples, electrochemical impedance spectroscopy (EIS) was conducted to identify the relationship between the electrochemical performance and electrode kinetics. Figure 5f shows the Nyquist plots for all cycled cells, which share the common feature of a depressed semicircle at high/medium frequency and an inclined line at low frequency. Apparently, the diameter of the semicircle for the Fe_3O_4/3DHPC-79 electrode is significantly smaller than those of other electrodes. This is clear evidence that Fe_3O_4/3DHPC-79 possesses the highest electrical contact and the fastest charge-transfer reaction for Li^+ insertion/extraction among all samples; it confirmed again the highly efficient combination of the matrix and Fe_3O_4 NPs.

To gain a deeper understanding of the excellent electrochemical performance of the Fe_3O_4/3DHPC-79 composite, we investigated the sample appearances and structure evolution before and after cycling by means of SEM and TEM. Fe_3O_4/3DHPC-65 and Fe_3O_4/3DHPC-79 electrodes nearly maintained their initial appearance; whereas the electrodes prepared with Fe_3O_4/3DHPC-89 and Fe_3O_4/3DHPC-E-79 suffered from loosening and sloughing off from the current collector during the cleaning process (Figure 6a–e). Furthermore, the SEM observations indicated that the overall 3D architecture of the cycled Fe_3O_4/3DHPC-65 could be generally retained after 500 cycles (Figure 6f, g). The magnified SEM and TEM images also showed substantial uniform spheres with a diameter around 190 nm (Figure 6h, i). However, in the case of Fe_3O_4/3DHPC-E-79 electrode (Figure S6 in the Supporting Information), it was crushed and severely aggregated, and numerous spherical particles around 1.3 μm were found after charging. Therefore, we speculate that the uneven distribution of Fe_3O_4 NPs in the 3DHPC network causes severe mechanical disintegration during cycling, thereby resulting in crumbling and cracking of the electrode and further electrical disconnection from current collectors. In addition, the aggregation of Fe_3O_4 particles leads to a significant reduction in the active surface area, while at the same time, the electrical contact with the carbon matrix also deteriorates, thereby resulting in significant capacity fading.

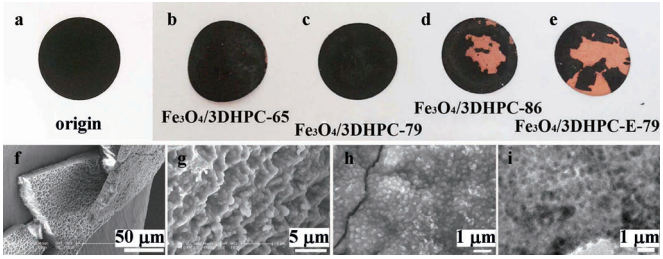

Figure 6. Digital photographs of Fe_3O_4/3DHPC composites a) before and b–e) after cycling; f–h) SEM and i) TEM images of the cycled Fe_3O_4/3DHPC-65 composite at different magnifications after 500 cycles at 2 A g^{-1}.

As shown by the results presented above, the Fe_3O_4/3DHPC-79 composite electrode displays excellent electrochemical performance and structural stability. These outstanding properties should be attributed to their distinct structure and the appropriate thickness of Fe_3O_4 NPs that offer the following benefits: 1) The open 3D macroporous carbon with interconnected mesoporous walls provides a large amount of available surface sites for Li^+ insertion, which facilitates physical contact with the electrolyte and provides fast Li^+ ion transport channels. 2) The present synthetic method guarantees that almost all Fe_3O_4 NPs are in intimate contact with the conductive support and improve the electron conductivity and utilize the electrochemical activity of the active material to the greatest possible degree, consequently conducting a complete redox process. 3) The intimate contact of Fe_3O_4 with the 3DHPC matrix is beneficial for mitigating the mechanical stress of Fe_3O_4 NPs generated during the charge/discharge process and preventing the aggregation of Fe_3O_4, and thus maintaining the structural integrity and cycling stability of the electrode. On the basis of the above analyses, it is concluded that the synergetic effect between 3DHPC and Fe_3O_4 NPs is responsible for the excellent lithium-storage performance of the overall electrode.

Conclusion

In summary, a new type of Fe_3O_4/3DHPC hybrid with small and uniform Fe_3O_4 NPs distributed on the 3DHPC support has been successfully synthesized by a simple, highly efficient, and green deposition technique assisted by a $scCO_2$-expanded ethanol solution. With the present method, the carbon-based matrix could be directly used without pretreatment or surfactant. In addition, the Fe_3O_4 content (or thickness) in the composite could be precisely tailored, and free Fe_3O_4 NPs formed in solution were successfully avoided. As a result, the Fe_3O_4/3DHPC-79 hybrid exhibited remarkable reversible capacity, excellent cycling performance, and good rate capability. The enhanced electrochemical performance can be attributed to the

synergistic effect between Fe_3O_4 NPs and the 3DHPC matrix. Finally, it should be pointed out that the present simple, straightforward, and environmentally benign synthetic method could be further extended to the fabrication of a wide range of functional hybrid nanomaterials.

Experimental Section

Materials synthesis

Nearly monodisperse silica nanospheres with a diameter of 200 nm were synthesized by Stober's method.[29] 3DHPC was synthesized according to a previously reported method.[18] As a typical procedure to prepare the Fe_3O_4/3DHPC composite, 3DHPC (20 mg) was dispersed in alcohol (10 mL) to form a suspension by ultrasonication, followed by adding a certain amount of $Fe(NO_3)_3{\cdot}9H_2O$ into the above solution with continuous magnetic stirring for 30 min. The obtained solution was transferred into a 50 mL Teflon-lined stainless-steel high-pressure autoclave. Subsequently, the vessel was placed into an oil bath at 200 °C and then pumped with CO_2 immediately up to 12.0 MPa with a flow rate of 10 mL min^{-1} under vigorous stirring. The final pressure reached approximately 20 MPa when the temperature reached equilibrium (note: be careful in handling process for scalding and leaking). After reaction for 2 h, the autoclave was cooled to room temperature naturally and then depressurized slowly. The resulting black solid products were centrifuged, washed with distilled water and ethanol, dried at 80 °C in air, and finally calcined at 550 °C for 3 h under an N_2 atmosphere with a ramp of 3 °C min^{-1}. The Fe_3O_4 content in the composite can be tailored to be 65, 79, and 86 wt% by adjusting the concentration of $Fe(NO_3)_3{\cdot}9H_2O$ in the precursor solution (Figure S1 in the Supporting Information), and the resulting composite was denoted as Fe_3O_4/3DHPC-X, with X representing the loading level. To compare and elucidate the efficiency of $scCO_2$, Fe_3O_4/3DHPC-E-79 composite was also prepared; 79 indicates the Fe_3O_4 content is 79 wt% in the composite, and E represents preparation in pure ethanol without introducing CO_2 under the same procedure.

Characterization

The crystal structure of the samples was characterized using X-ray diffraction (Bruker D8 Advance diffractometer using $Cu_{K\alpha}$ radiation ($\lambda = 1.5418$ Å)). XPS was recorded using a PHI quantera SXM spectrometer with an $Al_{K\alpha} = 280.00$ eV excitation source. The morphology and microstructure were analyzed using scanning electron microscopy (Hitachi S-4800) equipped with energy-dispersive X-ray spectroscopy (EDS). TEM and HRTEM were recorded using a Tecnai G20 instrument operating at 200 kV for the detailed microstructure information. Thermogravimetric analysis (TGA) was performed using a TGA 2050 thermogravimetric analyzer up to 800 °C at a heating rate of 10 °C min^{-1} in air. Nitrogen adsorption–desorption isotherms were measured at 77 K using a Micromeritics ASAP 2020 analyzer (USA).

Electrochemical characterization

The electrochemical tests were measured using two-electrode CR2025-type coin cells assembled in an argon-filled glovebox with lithium sheet as counter and reference electrode, 1.0 M $LiPF_6$ in ethylene carbonate (EC)/dimethyl carbonate (DMC) (1:1 in volume) as electrolyte, and Celgard-2300 polypropylene as separator. The working electrode was prepared by mixing the as-prepared active material with acetylene black (AB) and polyvinylidene fluoride (PVDF) at a weight ratio of 75:10:15. The resultant slurry was then cast uniformly on a copper foil current collector and dried at 80 °C for 2 h in air, and then at 100 °C in vacuum overnight. The weight of every electrode was weighed accurately using an electronic balance. The thickness of the electrode material was about 15 μm. The loading of the electrode was about 1–2 mg cm^{-2}. The charge/discharge measurements were performed at various current densities with a cutoff voltage of 0.01–3.0 V using a NEWARE cell test instrument (Shenzhen Neware Electronic Co., China). After cycling, the cell was disassembled in the glovebox, and the working electrode was taken out and washed with pure DMC solution for characterizations. Note that the specific capacity of the Fe_3O_4/3DHPC composites was calculated on the basis of the total weight of the composite. Cyclic voltammetry and electrochemical impedance spectroscopy (EIS) measurements were performed by using a VMP3 Electrochemical Workstation (Bio-logic Inc).

Acknowledgements

This work was financially supported by the One Hundred Talent Program of the Chinese Academy of Sciences and the NSFC (21273222).

Keywords: electrochemistry · iron oxide · nanoparticles · organic–inorganic hybrid composites · supercritical fluids

[1] P. Poizot, S. Laruelle, S. Grugeon, L. Dupont, J. M. Tarascon, *Nature* **2000**, *407*, 496–499.

[2] a) L. Yu, G. Q. Zhang, C. Z. Yuan, X. W. Lou, *Chem. Commun.* **2013**, *49*, 137–139; b) L. Li, K. H. Seng, Z. Chen, Z. Guo, H. K. Liu, *Nanoscale* **2013**, *5*, 1922–1928; c) Y. Wang, Y. J. Bai, X. Li, Y. Y. Feng, H. J. Zhang, *Chem. Eur. J.* **2013**, *19*, 3340–3347; d) J. Liu, W. Liu, K. F. Chen, S. M. Ji, Y. C. Zhou, Y. L. Wan, D. F. Xue, P. Hodgson, Y. C. Li, *Chem. Eur. J.* **2013**, *19*, 9811–9816; e) L. Li, T. T. Wang, L. Y. Zhang, Z. M. Su, C. G. Wang, R. S. Wang, *Chem. Eur. J.* **2012**, *18*, 11417–11422; f) L. Zhang, H. B. Wu, X. W. Lou, *Adv. Energy Mater.* **2013**, DOI: 10.1002/aenm.201300958; g) B. Wang, H. B. Wu, L. Zhang, X. W. Lou, *Angew. Chem. Int. Ed.* **2013**, *52*, 4165–4168; h) L. Zhang, H. B. Wu, S. Madhavi, H. H. Hng, X. W. Lou, *J. Am. Chem. Soc.* **2012**, *134*, 17388–17391.

[3] a) Y. Gong, S. Yang, Z. Liu, L. Ma, R. Vajtai, P. M. Ajayan, *Adv. Mater.* **2013**, *25*, 3979–3984; b) J. Z. Wang, C. Zhong, D. Wexler, N. H. Idris, Z. X. Wang, L. Q. Chen, H. K. Liu, *Chem. Eur. J.* **2011**, *17*, 661–667; c) T. Zhu, J. S. Chen, X. W. Lou, *J. Phys. Chem. C* **2011**, *115*, 9814–9820; d) J. S. Chen, Y. M. Zhang, X. W. Lou, *ACS Appl. Mater. Interfaces* **2011**, *3*, 3276–3279.

[4] Z. S. Wu, W. C. Ren, L. Wen, L. B. Gao, J. P. Zhao, Z. P. Chen, G. M. Zhou, F. Li, H. M. Cheng, *ACS Nano* **2010**, *4*, 3187–3194.

[5] a) Y. Chen, B. Song, L. Lu, J. Xue, *Nanoscale* **2013**, *5*, 6797–6803; b) F. Zhang, T. F. Zhang, X. Yang, L. Zhang, K. Leng, Y. Huang, Y. S. Chen, *Energy Environ. Sci.* **2013**, *6*, 1623–1632.

[6] a) Z. Y. Wang, D. Y. Luan, S. Madhavi, Y. Hu, X. W. Lou, *Energy Environ. Sci.* **2012**, *5*, 5252–5256; b) G. M. Zhou, D. W. Wang, F. Li, L. L. Zhang, N. Li, Z. S. Wu, L. Wen, G. Q. Lu, H. M. Cheng, *Chem. Mater.* **2010**, *22*, 5306–5313; c) J. L. Cheng, B. Wang, C. M. Park, Y. P. Wu, H. T. Huang, F. D. Nie, *Chem. Eur. J.* **2013**, *19*, 9866–9874.

[7] a) E. Kang, Y. S. Jung, A. S. Cavanagh, G. H. Kim, S. M. George, A. C. Dillon, J. K. Kim, J. Lee, *Adv. Funct. Mater.* **2011**, *21*, 2430–2438; b) M. B. Zheng, D. F. Qiu, B. Zhao, L. Y. Ma, X. R. Wang, Z. X. Lin, L. J. Pan, Y. D. Zheng, Y. Shi, *RSC Adv.* **2013**, *3*, 699–703; c) N. Yang, S. Zhu, D. Zhang, S. Xu, *Mater. Lett.* **2008**, *62*, 645–647; d) J. S. Zhou, H. H. Song, L. L. Ma, X. H. Chen, *RSC Adv.* **2011**, *1*, 782–791.

[8] a) L. H. Zhuo, Y. Q. Wu, J. Ming, L. Y. Wang, Y. C. Yu, X. B. Zhang, F. Y. Zhao, *J. Mater. Chem. A* **2013**, *1*, 1141–1147; b) R. R. Salunkhe, K. Jang, S. W. Lee, S. Yu, H. Ahn, *J. Mater. Chem.* **2012**, *22*, 21630–21635; c) G. L. Cui, L. Gu, N. Kaskhedikar, P. A. van Aken, J. Maier, *Electrochim. Acta*

2010, *55*, 985 – 988; d) C. Y. Li, L. Y. Li, W. W. Cai, S. L. Kodjie, K. K. Tenneti, *Adv. Mater.* **2005**, *17*, 1198 – 1202.

[9] a) Z. Y. Sun, X. R. Zhang, B. X. Han, Y. Y. Wu, G. M. An, Z. M. Liu, S. D. Miao, Z. J. Miao, *Carbon* **2007**, *45*, 2589 – 2596; b) T. Hanrath, B. A. Korgel, *J. Am. Chem. Soc.* **2002**, *124*, 1424 – 1429; c) L. Wang, Y. Zhao, Q. Y. Lai, Y. J. Hao, *J. Alloys Compd.* **2010**, *495*, 82 – 87.

[10] a) H. Yuvaraj, E. Park, Y. Gal, K. Lim, *Colloids Surf. A* **2008**, *313 – 314*, 300 – 303; b) X. R. Ye, Y. H. Lin, C. M. Wang, M. H. Engelhard, Y. Wang, C. M. Wai, *J. Mater. Chem.* **2004**, *14*, 908 – 913.

[11] a) W. Fan, W. Gao, C. Zhang, W. W. Tjiu, J. S. Pan, T. X. Liu, *J. Mater. Chem.* **2012**, *22*, 25108 – 25115; b) J. Zheng, Z. Q. Liu, X. S. Zhao, M. Liu, X. Liu, W. Chu, *Nanotechnology* **2012**, *23*, 165601 – 165608.

[12] a) Z. M. Liu, B. X. Han, *Adv. Mater.* **2009**, *13*, 825 – 829; b) F. Cansell, C. Aymonier, *J. Supercrit. Fluids* **2009**, *47*, 508 – 516; c) E. Reverchon, R. Adami, *J. Supercrit. Fluids* **2006**, *37*, 1 – 22.

[13] a) A. I. Cooper, *Adv. Mater.* **2003**, *15*, 1049 – 1059; b) J. Z. Yin, X. Z. Zhang, Q. Q. Xu, C. J. Zhang, A. Q. Wang, *Progress in Chem.* **2009**, *21*, 606 – 614.

[14] a) C. Erkey, *J. Supercrit. Fluids* **2009**, *47*, 517 – 522; b) Y. Xie, C. L. Zhang, S. D. Miao, Z. M. Liu, K. L. Ding, Z. J. Miao, G. M. An, Z. Z. Yang, *J. Colloid Interface Sci.* **2008**, *318*, 110 – 115; c) Z. Y. Sun, Z. M. Liu, B. X. Han, G. M. An, *Mater. Lett.* **2007**, *61*, 4565 – 4568; d) J. Ming, C. Y. Wu, H. Y. Cheng, Y. C. Yu, F. Y. Zhao, *J. Supercrit. Fluids* **2011**, *57*, 137 – 142; e) C. A. Eckert, B. L. Knutson, P. G. Debenedetti, *Nature* **1996**, *383*, 313 – 318.

[15] H. J. Fan, Q. Xu, J. G. Li, Y. X. Cao, *J. Am. Ceram. Soc.* **2006**, *89*, 3065 – 3069.

[16] C. N. He, S. Wu, N. Q. Zhao, C. S. Shi, E. Z. Liu, J. J. Li, *ACS nano* **2013**, *7*, 4459 – 4469.

[17] a) L. Estevez, R. Dua, N. Bhandari, A. Ramanujapuram, P. Wang, E. P. Giannelis, *Energy Environ. Sci.* **2013**, *6*, 1785 – 1790; b) N. Brun, S. R. S. Prabaharan, C. Surcin, M. Morcrette, H. Deleuze, M. Birot, O. Babot, M. F. Achard, R. Backov, *J. Phys. Chem. C* **2012**, *116*, 1408 – 1421.

[18] Y. H. Deng, C. Liu, T. Yu, F. Liu, F. Q. Zhang, Y. Wan, L. J. Zhang, C. C. Wang, B. Tu, P. A. Webley, H. T. Wang, D. Y. Zhao, *Chem. Mater.* **2007**, *19*, 3271 – 3277.

[19] J. Ming, H. Y. Cheng, Y. C. Yu, Y. Q. Wu, F. Y. Zhao, *J. Mater. Chem.* **2011**, *21*, 6654 – 6659.

[20] W. Sun, S. X. Zhou, B. You, L. M. Wu, *Chem. Mater.* **2012**, *24*, 3800 – 3810.

[21] a) L. L. Wang, J. W. Liang, Y. C. Zhu, T. Mei, X. Zhang, Q. Yang, Y. T. Qian, *Nanoscale* **2013**, *5*, 3627 – 3631; b) G. Q. Xie, P. X. Xi, H. Y. Liu, F. J. Chen, L. Huang, Y. J. Shi, F. P. Hou, Z. Z. Zeng, C. W. Shao, J. Wang, *J. Mater. Chem.* **2012**, *22*, 1033 – 1039; c) L. L. Li, Y. Chu, Y. Liu, L. H. Dong, *J. Phys. Chem. C* **2007**, *111*, 2123 – 2127.

[22] L. H. Zhuo, Y. Q. Wu, L. Y. Wang, J. Ming, Y. C. Yu, X. B. Zhang, F. Y. Zhao, *J. Mater. Chem. A* **2013**, *1*, 3954 – 3960.

[23] a) C. D. Wang, Q. M. Zhang, Q. H. Wu, T. W. Ng, T. L. Wong, J. G. Ren, Z. C. Shi, C. S. Lee, S. T. Lee, W. J. Zhang, *RSC Adv.* **2012**, *2*, 10680 – 10688; b) J. E. Lee, S. H. Yu, D. J. Lee, D. C. Lee, S. I. Han, Y. E. Sung, T. Hyeon, *Energy Environ. Sci.* **2012**, *5*, 9528 – 9533.

[24] Y. He, L. Huang, J. S. Cai, X. M. Zheng, S. G. Sun, *Electrochim. Acta* **2010**, *55*, 1140 – 1144.

[25] H. Wu, N. Du, J. Z. Wang, H. Zhang, D. R. Yang, *J. Power Sources* **2014**, *246*, 198 – 203.

[26] J. S. Xu, Y. J. Zhu, *ACS Appl. Mater. Interfaces* **2012**, *4*, 4752 – 4757.

[27] S. Laruelle, S. Grugeon, P. Poizot, M. Dollé, L. Dupont, J. M. Tarascon, *J. Electrochem. Soc.* **2002**, *149*, A627 – A634.

[28] Y. Li, Z. Y. Fu, B. L. Su, *Adv. Funct. Mater.* **2012**, *22*, 4634 – 4667.

[29] W. Stöber, A. Fink, *J. Colloid Interface Sci.* **1968**, *26*, 62 – 69.

Received: December 1, 2013
Published online on March 3, 2014